Biotransformation of Silver Released from Nanoparticle Coated Titanium Implants Revealed in Regenerating Bone

ACS APPLIED MATERIALS & INTERFACES

Research Article

www.acsami.org

Biotransformation of Silver Released from Nanoparticle Coated Titanium Implants Revealed in Regenerating Bone

Hua Geng,[†,‡] Gowsihan Poologasundarampillai,[†,‡] Naomi Todd,[§] Aine Devlin-Mullin,[§] Katie L. Moore,[†] Zahra Golrokhi,[∥] James B. Gilchrist,[‡] Eric Jones,[∥] Richard J. Potter,[∥] Chris Sutcliffe,[∥] Marie O'Brien,[†] David W.L. Hukins,[⊥] Sarah Cartmell,[†] Christopher A. Mitchell,[§] and Peter D. Lee*[,†,‡]

[†]School of Materials, The University of Manchester, Oxford Road, Manchester M13 9PL, U.K.

[‡]Research Complex at Harwell, Harwell OX11 0FA, U.K.

[§]Centre for Molecular Biosciences (CMB), School of Biomedical Sciences, Ulster University, Coleraine BT52 1SA, Northern Ireland

[∥]Centre for Materials and Structures, School of Engineering, The University of Liverpool, Liverpool L69 3GH, U.K.

[⊥]Department of Mechanical Engineering, School of Engineering, University of Birmingham, Birmingham B15 2TT, U.K.

ABSTRACT: Antimicrobial silver nanoparticle coatings have attracted interest for reducing prosthetic joint infection. However, few studies report in vivo investigations of the biotransformation of silver nanoparticles within the regenerating tissue and its impact on bone formation. We present a longitudinal investigation of the osseointegration of silver nanoparticle-coated additive manufactured titanium implants in rat tibial defects. Correlative imaging at different time points using nanoscale secondary ion mass spectrometry, transmission electron microscopy (TEM), histomorphometry, and 3D X-ray microcomputed tomography provided quantitative insight from the nano- to macroscales. The quality and quantity of newly formed bone is comparable between the uncoated and silver coated implants. The newly formed bone demonstrates a trabecular morphology with bone being located at the implant surface, and at a distance, at two weeks. Nanoscale elemental mapping of the bone–implant interface showed that silver was present primarily in the osseous tissue and colocalized with sulfur. TEM revealed silver sulfide nanoparticles in the newly regenerated bone, presenting strong evidence that the previously in vitro observed biotransformation of silver to silver sulfide occurs in vivo.

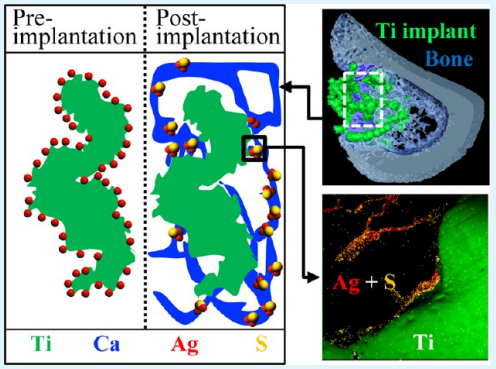

KEYWORDS: *silver nanoparticle coatings, atomic layer deposition, biotransformation, bone formation, osseointegration*

1. INTRODUCTION

Additive manufactured (AM) open-porous titanium implants[1,2] are increasingly used in orthopedic applications where bone fixation and load bearing are required. These open-porous implants allow desirable early bone ingrowth[3] and more rapid osseointegration.[4,5] Unfortunately, the placement of prostheses is also associated with the risk of prosthetic joint infection (PJI),[6,7] ultimately leading to delayed healing or implant failure. It has been estimated that 2.5% of patients with primary knee and up to 20% of revision knee replacements have been affected by PJI.[8,9] Treatment of such infection with antibiotics proves to be ineffective due to biofilm formation with the ability of the immune system to respond also being hampered.[10,11] Therefore, an antimicrobial surface aimed at preventing the bacterial colonization and biofilm formation during surgery and in the immediate postoperative period is highly desirable.

Silver-based antimicrobials are of particular interest due to their broad antimicrobial spectrum and efficacy,[12,13] allowing them to inhibit both Gram-positive and Gram-negative bacteria with very low silver concentrations. Nanoscale silver (nano-Ag) such as silver nanoparticles (AgNPs) is more reactive than its bulk counterparts due to the large surface area-to-volume ratio.[14] The interaction of AgNPs with moisture and body fluid leads to the fast release of biologically active silver ions,[15] binding to bacterial protein or DNA[16] and thereby preventing bacterial adhesion and biofilm formation. In addition, ultrathin AgNP films have been successfully incorporated onto non-planar surfaces and complex architectures by several techniques.[17−19] Atomic layer deposition (ALD), a sequential and self-limiting process, provides a number of advantages for depositing an AgNP surface layer, including texturing and biocompatibility. The sub-angstrom control of silver deposition coupled with the self-saturating reaction lead to the formation of uniform sized AgNPs coated onto the additive manufactured porous titanium.[17] In a previous study, ALD of silver coated Ti implants was shown to be effective in reducing major pathogenic biofilm formation in vitro.[20]

The remarkable antimicrobial effects of AgNPs have led to their application in a diverse range of orthopedic implants. However, the close contact that exists between silver coated

Received: April 12, 2017
Accepted: June 5, 2017
Published: June 5, 2017

DOI: 10.1021/acsami.7b05150
ACS Appl. Mater. Interfaces 2017, 9, 21169−21180

implants and bone[21] also raises concerns regarding the potentially harmful effect associated with the uptake of the silver ions into bone and surrounding soft tissue.[22] AgNPs can readily penetrate the cell membrane,[23] releasing ions locally to a specific tissue[24] and becoming internalized.[25,26] Therefore, a detailed study on the impact of AgNPs is required.

Considerable effort has been expended in examining the biological effect of silver on bone using a variety of cell lines, and it has been shown that the impact of AgNPs is both size-[27,28] and dose-dependent.[29−33] These in vitro studies provide an understanding of silver interaction with the specific cell types involved in bone healing, revealing a potential reduction in possible harmful effects by controlling the initial total amount of silver. Further, recent in vitro evidence suggests that the silver undergoes sulfidation to silver sulfide[34] through complex interactions with protein (serum) and cells.[35] This lead to the hypothesis that the biological toxicity of silver is reduced through the biotransformation of silver into silver sulfide, a more stable and less toxic compound.[35] However, the cellular response triggered by silver and its sulfidation to silver sulfide in vitro cannot be directly used to predict tissue level response in vivo. Bone healing, when augmented by implants, is characterized by complex interactions between multiple cell types and the osteoconductive properties of the material,[36−39] all of which could be disrupted by silver.

In the majority of prior studies, there is a lack of information dealing with the harmful effects of silver on bone regeneration with apparent inconsistencies in the results obtained. Korani et al.[40] observed an abnormal inflammatory response in lamellar bone following the dermal exposure of silver. On the contrary, Marsich et al.[41] found comparable bone healing patterns without significant difference in bone contact. These contradictory results may be explained by the differences in routes of exposure (e.g., bone contact, blood contact, or inhalation) and experiment end-point, inevitably raising doubts about whether silver coating is detrimental to bone healing.

To date, only a few studies have focused on the effect of silver on bone regeneration associated with implanted materials.[41,42] However, none have performed investigations examining multiple time-points during incorporation of implants nor have they assessed the uptake/distribution of silver in tissue upon release from an implant. These aforementioned experiments can provide particularly useful information regarding the possible biological effect of silver on bone healing and potential target tissue following the contact of new bone and silver coated devices, respectively. For these reasons, detailed in vivo studies are required to fully elucidate the impact of silver on bone healing.

In the present study, the quantity and quality of bone following surgical implantation of both silver coated and uncoated titanium scaffolds were assessed using both X-ray microcomputed tomography (μCT) and histological measurements. The impact of silver coating was assessed after 2, 6, and 12 weeks in vivo to identify whether the presence of silver affects bone healing or decreases new bone generation. The distributions of released silver ($^{107}Ag^-$) in addition to $^{12}C^-$, $^{40}Ca^{16}O^-$,$^{31}P^{12}C^-$, and $^{32}S^-$ within adjacent tissues were quantified using nanoscale secondary ion mass spectrometry (NanoSIMS). Transmission electron microscopy (TEM) and selected area electron diffraction (SAED) were combined to examine the newly formed bone. Correlative imaging was used to combine all of these complementary techniques to investigate the bone−implant interface and the biotransformation of the silver.

2. MATERIALS AND METHODS

2.1. Fabrication and Preparation of the Open-Porous Implants. Open-porous titanium implants were fabricated by additive manufacturing as previously described.[43] Briefly, cylindrical shaped titanium implants of 2.5 mm diameter and 1.5 mm height, as shown in Figure 1a, were produced using a MCP Realizer 250 selective laser

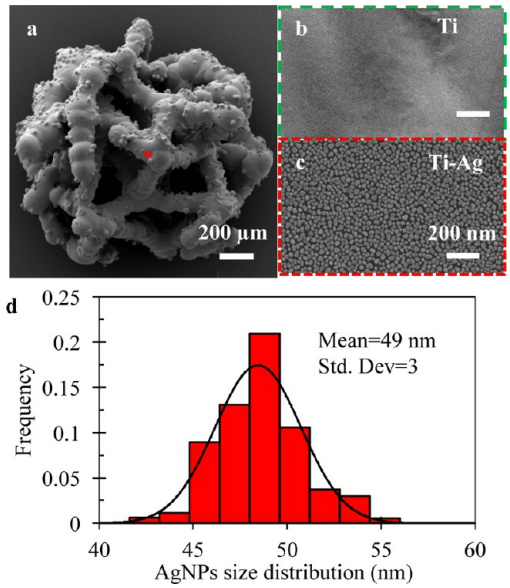

Figure 1. (a) Macroscopic SEM-SE image of the additively manufactured porous titanium scaffold. High-resolution SEM images of (b) titanium scaffolds and (c) silver coated titanium scaffolds. (d) Size distribution histogram of silver particles (125 °C for 500 ALD cycles).

melting (SLM) system (MCP Tooling Technologies, Lubeck, Germany). The basic material used to fabricate implants was grade 1 commercially pure titanium (CP-Ti) powder with a modal particle diameter of 28.5 μm (Sumitomo Corp., Tokyo, Japan).[43] The powder layer thickness used in the build process was 50 μm.[43] The open-porous implants were made with a nominal porosity of 65% and a strut diameter of 180 μm.[2]

Following the SLM build process, the implants were cleaned in an ultrasonic bath (VWR, Radnor, United States) with micro-90 detergent (Decon, Sussex, UK) diluted 1:20 in distilled water to remove unfused powder. The samples were then rinsed in distilled water and dried. Once cleaned, the samples were subject to heat treatment in an inert atmosphere at 667 Pa and 1400 °C (for 3 h). Before atomic layer deposition, the sintered implants were once again sintered and cleaned using the process described above.

2.2. ALD of the AgNP Coating. Surface modification of the implant samples with an ultrathin layer of silver was carried out using direct liquid injection ALD in a customized Aixtron AIX 200FE AVD reactor.[20] The ALD process used has been shown to be controlled by self-limiting surface reactions, enabling the production of highly conformal nanotextured metallic silver films on complex three-dimensional structures.[44,17] The organometallic precursor and coreactant used in the deposition process was (hexafluoroacetylacetonato)silver(I)(1,5-cyclooctadiene) dissolved in a 0.1 M anhydrous toluene solution (Sigma-Aldrich, Germany) and propan-1-ol (HPLC grade/Fisher, Leics, UK), respectively. Each ALD cycle consisted of a 4 step process, starting with a 4 s dose of the silver precursors, followed by an 8 s argon (99.999%; BOC, UK) purge, a 4 s propan-1-ol dose, and finally another 8 s argon purge. The silver precursor solution was introduced into the reactor using direct liquid

DOI: 10.1021/acsami.7b05150
ACS Appl. Mater. Interfaces 2017, 9, 21169−21180

injection at a rate of 17.5 μL/s and was volatilized at 130 °C, while the propan-1-ol was delivered into the reactor from a vapor-draw bottle held at room temperature (~20 °C) using a Swagelok ALD valve. Each sample was coated using 500 ALD cycles to give a nominal film thickness (if uniform rather than particulate islands) of ~13 nm, which corresponds to a rate of 0.026 nm/cycle.

2.3. Scanning Electron Microscopy. The structure of the Ti and Ti−Ag implants was characterized by scanning electron microscopy (JEOL JSM-7001F FEG-SEM, Tokyo, Japan) in secondary electron mode using a 10 kV accelerating voltage.

2.4. Sterilization. Before implantation, all samples were soaked in ethanol for 2 h before sterilization with ultraviolet (UV) light in a Class II biosafety cabinet (Esco, Canada).[45]

2.5. Surgical Implantation. A total of 36 adult male Wistar rats, 10−12 weeks old and weighting 300−400 g, were used for the in vivo study. The experimental protocol was approved by the institutional animal care committee at the University of Ulster and National (UK Home Office) guidelines. In brief, an anesthetic drug (2.0 mL Ketaset, 100 mL/mg) and 1.0 mL Xylapan (20 mL/mg) diluted in 5 mL phosphate buffered saline (PBS) (pH 7.4, 0.5 mL/100 g) was injected to sedate the animals. For the surgical procedures, a 2.5 mm subcritical size defect was created using a trephine bur. The circular defect penetrated well into the marrow cavity. Rats were randomly divided into two groups of 18 rats each implanted with titanium (Ti) or silver coated titanium implants (Ti−Ag).

After healing periods of 2, 6, and 12 weeks, the animals were sacrificed, and the implanted tibiae were subsequently fixed in a solution of 10% buffered formal saline for X-ray μCT scanning.

2.6. Ex Vivo X-ray μCT. *2.6.1. Image Acquisition.* Post-implantation, all implanted tibiae (n = 36) were wrapped in Parafilm M (Bemis, United States) and placed in an ABS plastic tube. The scanning was performed using a laboratory-based μCT system (Nanofocus, Phoenix|X-ray General Electric Company, Measurement and Control, Wunstorf, Germany). To reduce beam hardening artifacts,[37] the μCT scanner was operated at 85 kV and 111 μA with a 0.5 mm-thick copper filter. Images were reconstructed using the Datos|x software (Phoenix|X-ray), resulting in an image matrix of 990 × 990 × 1000 pixels with an isotropic voxel size of 5 μm. The reconstructed images were subsequently analyzed in Avizo software (Avizo 8.0, FEI Visualization Sciences Group, Mérignac Cedex, France) and Matlab (Mathworks Inc., Natick, Massachusetts, United States).

2.6.2. Segmentation. The segmentation procedure comprised an image filter, a global threshold, and a local thresholding method.[46] In the first pass, the reconstructed data were normalized to a predetermined reference histogram before undergoing smoothing filters (edge preserving filter and anisotropic diffusion filter)[47] to reduce the influence of noise and artifacts. The filtered images were first presegmented into a "mask" containing bone and implant areas using an Ostu algorithm.[46] After presegmentation, the bone was segmented from the implant area using local thresholding.[46] The boundary between the bone and implant was smoothed using the morphological operations of erosion (by one pixel) and dilation (by one pixel).

2.6.3. Quantification of the Titanium Scaffold and Newly Formed Bone. After segmentation, the bone and titanium phases from each individual sample were registered with a high resolution tibia shape model and a cylindrical mask (2.5 mm in diameter and 1.5 mm in height), respectively. The overlapping of the shape model and cylindrical mask were used to generate the region of interest (ROI) in a reproducible fashion (Figure 2a). Microarchitectural parameters (1) bone ingrowth (BI) [(bone area/ROI) × 100%], (2) bone contact (BC) [(bone contact area/total scaffold area) × 100%), (3) specific surface area (SSA) [(bone area/bone volume) × 100%], (4) bone trabecular thickness (Tb.Th), and (5) trabecular separation (Tb.Sp)[48] of the newly formed bone were analyzed within the defined ROI. Strut thickness and porosity of the titanium scaffolds were measured.[2,49]

2.7. Histology and Histomorphometry. Histological preparation of rat tibiae containing titanium implants has been previously described in detail.[50] Briefly, 18 tibial specimens containing the implants (n = 3 at 2, 6, and 12 weeks in the Ti and Ti−Ag groups) were decalcified, dehydrated, infiltrated and embedded in LR white resin (TAAB Laboratories Equipment Ltd., Berks, UK). The polymerized blocks were trimmed of excess resin and glued onto plastic microscope slides (EXAKT, Oklahoma City, United States). An EXAKT Vacuum Adhesive Press was used to mount the samples for UV treatment (5 min). Subsequently, one-half of the samples were cut approximately from the center of the Ti implant using an EXAKT 310 Macro Band System with a diamond blade (EXAKT). The blocks were ground successively with K800, K2500, and K4000 grinding paper (EXAKT) using an EXAKT 400CS grinding system to yield ~50−100 μm-thick sections. Finally, the sections were stained with Gill's Haematoxylin III (Fisher Scientific, Loughborough, UK) and multiple staining solution before examination on a Zeiss Axiophot microscope (Zeiss; Wetzlar, Germany). Histomorphometric analysis of new bone consisted of a quantitative assessment of the BI.

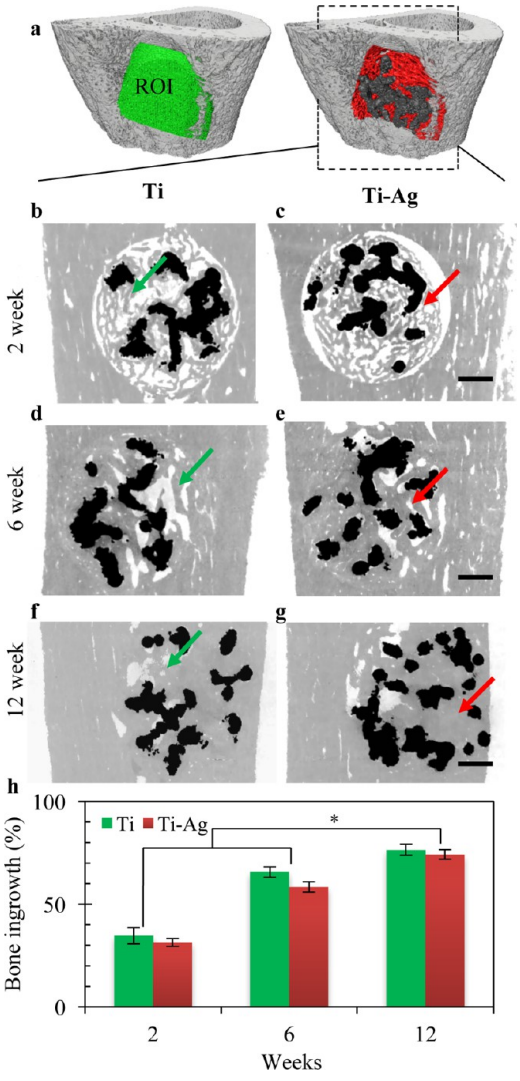

Figure 2. (a) X-ray μCT images of bone formation within the ROI. Bone ingrowth was quantified at (b and c) 2, (d and e) 6, and (f and g) 12 weeks postoperation. Arrows indicate the newly regenerated bone in the uncoated (green) and silver coated group (red). (h) The amount of bone ingrowth, expressed as the percentage bone volume within ROI as measured by μCT. Statistical significance (*) was considered where $p < 0.05$. Scale bars are 500 μm.

2.8. Sample Preparation for Spectroscopic Analyses. Four nondecalcified samples of tibia with implant (n = 1 at 2 weeks in the Ti group; n = 1 at 2, 6, and 12 weeks in the Ti−Ag group) were washed in distilled water and kept in a −80 °C freezer (New Brunswick

DOI: 10.1021/acsami.7b05150
ACS Appl. Mater. Interfaces 2017, 9, 21169−21180

Table 1. BI and BC Measured from μCT and Histology

	Ti			Ti−Ag		
	μCT		histology	μCT		histology
time (weeks)	BI (%)	BC (%)	BI (%)	BI (%)	BC (%)	BI (%)
2	35 ± 10	20 ± 6	31 ± 9	31 ± 5	14 ± 5	29 ± 8
6	66 ± 6	56 ± 10	42 ± 7	58 ± 7	44 ± 13	59 ± 15
12	76 ± 7	71 ± 11	77 ± 6	74 ± 6	73 ± 9	66 ± 10

Scientific, Enfield, United States) for 48 h. The frozen samples were then freeze-dried in a CoolSafe 100-4 freeze-drier (Scanvac-Coolsafe, Lynge, UK) for 48 h. At the end of the drying cycle, bone−implant samples were mounted in LR white resin (Sigma-Aldrich, Dorset, UK) and polished to a mirror finish using 1 μm diamond suspension paste (Struers, Glasgow, UK). Immediately before NanoSIMS analysis, the embedded samples were coated with 10 nm of platinum.

2.9. NanoSIMS. NanoSIMS images of the bone implant samples were acquired using a CAMECA NanoSIMS 50L instrument (Cameca, Gennevilliers Cedex, France). A 16 keV Cs^+ primary ion beam with a current of 1.8−2.6 pA was scanned over the surface to generate negative secondary ions. The instrument was calibrated using standards of high concentration to detect $^{12}C^-$, $^{32}S^-$, $^{31}P^{12}C^-$, $^{40}Ca^{16}O^-$, $^{48}Ti^{16}O^-$, and $^{107}Ag^-$. To ensure that each imaged area was at steady state and to remove the platinum coating, Cs^+ ions were implanted into the surface to achieve a dose of 1×10^{17} ions cm^{-2}. Six to eight regions of interest were imaged from each sample with an area of 50×50 μm^2 (512×512 pixels). A dwell time of 5000 μs/pixel was used with an aperture size of 300 μm (D1 = 2). Image processing was carried out using ImageJ software (United States National Institutes of Health, Bethesda, Maryland, United States) with OpenMIMS plugin (National Resource for Imaging Mass Spectrometry, Cambridge, Massachusetts, United States).

2.10. Sample Preparation for Correlative Imaging. After the NanoSIMS experiments, the surface that was analyzed with NanoSIMS was polished using a 6 μm diamond suspension (Struers, Glasgow, UK) and glued onto a glass slide (Thermo Scientific, Hudson, United States). The other side of the sample was further ground using K1200 and P4000 grinding paper (Struers, Glasgow, UK) until the sample was 70−90 μm thick. These sections were stained with Goldners Trichrome (method adapted from ref 51). Briefly, the sections were rinsed with distilled water for 15 min, and the nuclei were stained for 20 min using Weigert's Haematoxylin (Sigma-Aldrich, Dorset, UK). The sections were then rinsed with distilled water and stained with 0.01% azophloxine for 15 min. Sections were then rinsed with 1% acetic acid followed by staining with 2% Orange G for 3 min and rinsed again with 1% acetic acid. Lastly, they were stained with 0.2% Light Green for 5 min followed again by rinsing with 1% acetic acid for 5 min. The sections were then blotted dry and imaged using Olympus SZX16 stereoscopic microscope at a range of magnifications. The histological appearance of tissues in the images is consistent with mineralized bone staining green/dark green and fibrous tissue as orange/orange red.

1.11. TEM Imaging. The Goldners trichrome stained histological sections were polished to ∼30 μm using P4000 grinding paper (Struers, Glasgow, UK). The section was then mounted in a 3.05 mm Cu folding grid with a 1 mm circular hole in the center (Agar Scientific, UK). To thin the section to electron transparency a Fischione 1050 Ar^+ mill was used. Thinning was performed at successively lower beam energies and shallower angles (with respect to the section plane). Initial beam conditions were 10 kV and ±10°. Final thinning conditions were 4 kV and ±6°.

To differentiate the bone and fibrous tissue, the ion beam milled bone implant sample was imaged using a stereoscopic microscope (Olympus SZX16) at a range of magnifications. The sample was then imaged using a JEOL 2100 TEM operated at 200 kV. Images and diffraction patterns were acquired up to ∼5 μm from the implant surface. For imaging, a 1 s camera exposure time was used. For diffraction patterns, a ∼0.4 μm SA aperture and a 5 s camera exposure time were used.

2.12. Statistical Analyses. The results from μCT ($n = 6$) and histomorphometry analysis ($n = 3$) are presented as mean ± standard deviation. Statistical comparisons were performed with a Mann−Whitney U test. All statistical analysis was carried out using XLSTAT (Addinsoft, Inc., United States) with statistical significance considered when $p < 0.05$(*).

3. RESULTS

3.1. Characterization of the Open-Porous Titanium Implants. The Ti implants (Figure 1a) were found to have a porosity of 67 ± 5%, and the modal strut diameter was 170 ± 20 μm. This compares favorably with the original design, which aimed to have 65% porosity and 180 μm struts.[2] The selective laser melting (SLM) of the pure Ti powders gives rise to scaffolds (Figure 1b) with a rough surface, irregular shape, and a large surface area. During the ALD deposition process, metallic AgNPs (Figure 1c) are uniformly deposited on the porous Ti surface. From the size distribution histogram (Figure 1d), an average particle size of 49 ± 3 nm could be estimated.

3.2. Analysis of Quantity of Bone Using Ex Vivo X-ray Microcomputed Tomography. *3.2.1. Bone Ingrowth.* Three-dimensional μCT analysis of the entire implant was performed on 2, 6, and 12 week samples of rat tibia containing titanium scaffolds to assess bone ingrowth in a predefined ROI (Figure 2a). Representative μCT images (Figures 2b−g) qualitatively confirm bone formation progresses over time for both the uncoated and silver coated titanium scaffolds. New bone was observed at the edge and interior of the defect site at 2 weeks after implantation with 35 ± 10 and 31 ± 5% of void space being replaced by irregular immature bone (Figures 2b and c). At 6 weeks postimplantation, a higher proportion of new bone was detected along the porous titanium implant from the surface to the center (Figures 2d and e). After 12 weeks, the implant pores were almost completely filled by newly formed bone (Figures 2f and g). The results of the quantitative data measured from μCT are summarized in Table 1 and Figure 2h. No difference in bone ingrowth was observed between the Ti and Ti−Ag groups. There were significant statistical differences in bone ingrowth between 2 and 6 weeks and 2 and 12 weeks postimplantation ($p = 0.002$ and 0.001, respectively).

3.2.2. Bone Contact. The contact area in the Ti (green) and Ti−Ag (red) groups were shown in 3D (Figure 3a−f). An increase in bone contact length was observed as the healing period increased (from 2−12 weeks postimplantation) in both groups. The BC of the Ti (56 ± 10%) and the Ti−Ag group (44 ± 13%) at 6 weeks' postimplantation was significantly higher than at 2 weeks postimplantation (20 ± 6 and 14 ± 5%) ($p < 0.05$). After 12 weeks implantation, up to 82% of the implant surface was colonized by newly formed bone. Significant differences in BC were not observed between the titanium and silver coated groups. The quantitative measurements of the BC for both groups are summarized in Table 1 and Figure 3g.

DOI: 10.1021/acsami.7b05150
ACS Appl. Mater. Interfaces 2017, 9, 21169−21180

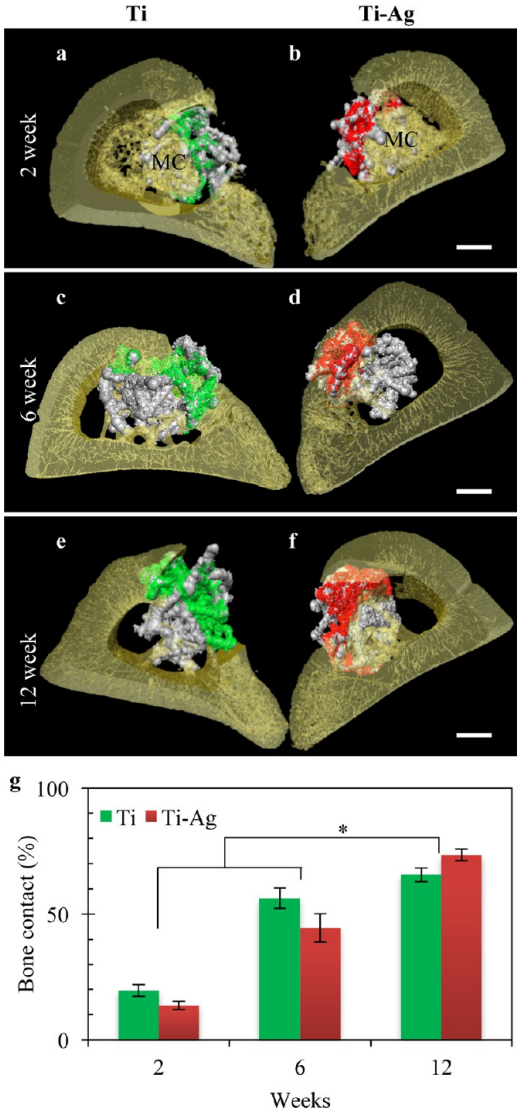

Figure 3. μCT images of bone to titanium scaffold contact with and without silver coating at (a and b) 2, (c and d) 6, and (e and f) 12 weeks postimplantation. (g) Bone contact, expressed as the percentage of bone implant contact within the ROI as measured by μCT. Statistical significance (*) was considered where $p < 0.05$. Scale bars are 500 μm.

3.2.3. Bone Morphometric parameters. We observed an increase in Tb.Th and a decrease in SSA and Tb.Sep as the healing period increased in both groups (Figure 4 and Table 2). The thickness of the newly formed bone was increased between 2 and 6 weeks and 2 and 12 weeks ($p < 0.05$). No significant differences in SSA, Tb.Th, or Tb.Sep were found between the uncoated and silver coated titanium groups. There was a significant decrease in SSA between 2 and 6 weeks and 2 and 12 weeks ($p < 0.05$). In the titanium implant, there were significant increase between 2 and 6 weeks (62 ± 8 and 102 ± 17 μm, $p < 0.05$) and 2 and 12 weeks (62 ± 8 and 122 ± 28 μm, $p < 0.05$) respectively for Tb.Th. In the silver coated titanium implant, the increase in Tb.Th was observed only between 2 (62 ± 24 μm) and 12 weeks (129 ± 25 μm).

3.3. Quality of Newly Formed Bone Using Histology and Histomorphometry. In the 2 week samples from the Ti and Ti–Ag groups, newly formed bone is seen on both the periphery of the defect as well as the surface of the implant,

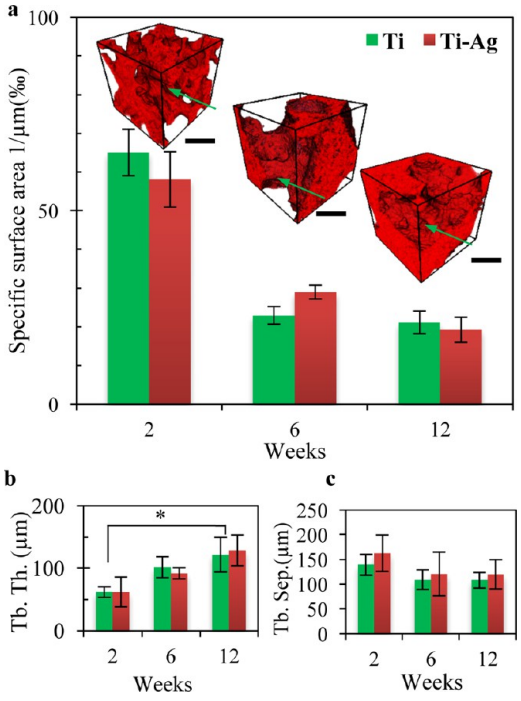

Figure 4. Bone morphometric parameters. (a) SSA, (b) Tb.Th, and (c) Tb.Sep as measured by μCT. Representative μCT images are inset in panel a. Statistical significance (*) was considered where $p < 0.05$. Scale bars are 200 μm.

where trabecula tended to be smaller in diameter and composed of woven bone (Figures 5a and b). At 6 weeks' postimplantation, lamellar bone is more conspicuous (Figures 5c and d). By 12 weeks, the gap between the implant and defect further decreased, and lamellar bone predominated (Figures 5e and f).

The histomorphometrical assessment of BI in the Ti and Ti–Ag group is summarized in Figure 5g and Table 1. In both groups, BI increased significantly between 2 and 12 weeks postimplantation ($p < 0.05$).

3.4. Elemental Mapping of Newly Formed Bone Using NanoSIMS. NanoSIMS analysis of the samples revealed local element distributions at the bone–implant interface at two weeks postimplantation in both the Ti (Figures 6a–e) and Ti–Ag groups (Figures 6f–j). Brighter regions of the images indicate higher counts for that elemental signal. Strong $^{40}Ca^{16}O^-$, $^{31}P^{12}C^-$, and $^{32}S^-$ signals were observed in the bone tissue; $^{48}Ti^{16}O^-$ signals were highest from the titanium implant, and $^{12}C^-$ was observed in certain areas at the bone–implant interface and presumably originates from organic fragments in the bone as well as the resin.

The heterogeneous distribution of $^{40}Ca^{16}O^-$ and $^{31}P^{12}C^-$ (Figures 6c–d and h–i, respectively) observed at 2 weeks' postimplantation over the trabecular network, represents a different degree of maturity of the newly formed bone. Bone growth in direct contact along the entire surface of the implant (contact osteogenesis) was observed in both groups, revealing osseointegration at early time points (Figures 6c and h).

The NanoSIMS elemental maps of $^{48}Ti^{16}O^-$, $^{40}Ca^{16}O^-$, $^{32}S^-$, and $^{107}Ag^-$ signals are given in Figure 7. The maps demonstrate the distribution of Ti (Figure 7i), Ca (Figure 7ii), S (Figure 7iii), and Ag (Figure 7iv), while the merged images (Figure 7v) of Ti, Ca, and Ag at the implant interface for 2 weeks for Ti and 2, 6, and 12 weeks for Ti–Ag show the interactions. As before,

DOI: 10.1021/acsami.7b05150
ACS Appl. Mater. Interfaces 2017, 9, 21169–21180

Table 2. Bone Morphometric Parameters Measured from X-ray μCT

	Ti			Ti–Ag		
time (weeks)	SSA (μm^{-1} ‰)	Tb.Th (μm)	Tb.Sep (μm)	SSA (μm^{-1} ‰)	Tb.Th (μm)	Tb.Sep (μm)
2	65 ± 6	62 ± 8	139 ± 21	58 ± 7	62 ± 24	163 ± 37
6	23 ± 2	102 ± 17	109 ± 20	29 ± 2	92 ± 9	121 ± 44
12	21 ± 3	122 ± 28	108 ± 16	19 ± 3	129 ± 25	120 ± 30

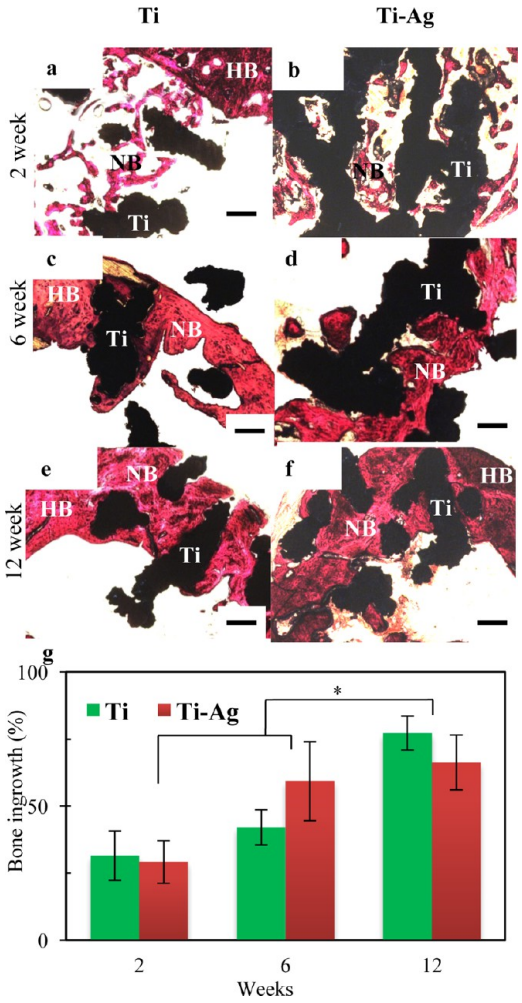

Figure 5. Representative histology images of hematoxylin and multiple stained bone–titanium implant sections at (a and b) 2, (c and d) 6, and (e and f) 12 weeks postimplantation. (g) Bone ingrowth in Ti and Ti–Ag groups (n = 3) is measured from histomorphometry. Statistical significance was considered where $p < 0.05$. Scale bars are 200 μm.

Ca and S intensities are highest at the bone tissue. Silver was detected in the Ti–Ag samples at all time points (Figures 7b–d(iv). The merged images (Figure 7v) reveal that silver is slowly released from the implant surface, as expected, but interestingly, some becomes confined within the newly formed osseous tissue. Furthermore, colocalization of silver and sulfur was observed, where the silver signal indicated by red arrows in Figures 7b–d(iv) was highest in regions with the high intensity sulfur signal (yellow arrows in Figures 7b–d(iii). Additionally, 2 weeks postimplantation, silver in the osseous tissue was observed both at the surface of the implant as well as in the trabecula away from the implant. But at 6 and 12 weeks, silver was found only at the bone attached to the surface of the implant (yellow arrowhead in Figure 7d(iii), red arrowhead in Figure 7d(iv)).

3.5. Correlative Imaging Using μCT, Histology, and NanoSIMS. Correlative multimodal imaging was used to quantify bone tissue within the whole defect site, to identify different tissues present in the bone-tissue interface, and to visualize their elemental makeup.

At 2 weeks postimplantation, the trabecular structure of the newly formed bone is clearly observed in the μCT image (Figure 8a). The histology image (Figure 8b) shows both the woven bone (green/dark green) and fibrous tissue (orange). The inset of histology (Figure 8b) shows a high magnification image of a 50 μm^2 region, and the corresponding NanoSIMS images of this region are shown in Figures 8c–g, revealing the Ti, Ca, S, and Ag maps within the implant and the newly formed tissue. Calcium and sulfur are observed in the newly formed bone, colocalized with silver content ($^{107}Ag^-$) both near and distant from the implants.

At 12 weeks postimplantation, the void space around the porous implant is filled by newly formed bone with significantly increased thickness revealed by the μCT image (Figure 8h). A region of less attenuating tissue was observed at the bone–implant interface (white arrowhead) which, when correlated to the magnified histology image (Figure 8i), reveals that fibrous tissue is still present at the interface. The colocalization of silver and sulfur in NanoSIMS images is observed only at the region near the bone–implant interface (Figures 8c–g).

3.6. TEM and SAED. TEM images and SAED patterns were collected from the bone implant interface region. Figure 9a shows a low magnification image of a region of silver coated titanium scaffold with tissue attached to the surface of the implant. The dotted purple line delineates the interface between titanium implant and tissue. Inset of Figure 9a shows the histological image of an electron transparent tissue region near the silver coated implants. Both bone (green) and fibrous (orange) tissues were identified in close proximity to each other adjacent to the implant surface. TEM micrographs from the bone region (white box, inset in Figure 9a) shows the distinctive ~10 nm width fibrillar structures (yellow arrows, Figures 9b and c) with particles (red arrows, Figures 9b and c) within these areas. Electron diffraction pattern (Figure 9d) from the area bounded by the circle reveals the crystalline nature of the sample.

4. DISCUSSION

Prosthetic joint infection (PJI) remains a serious complication after orthopedic surgery, which has led to a number of approaches being developed to modify bacterial adhesion and growth on the surfaces of implanted devices. AgNPs are effective in preventing bacterial adhesion, biofilm formation, and subsequent PJI.[14,16,20] An investigation by Liu et al.[63] into in vitro dissolution of AgNPS in biological medium showed a fast silver release profile up to 12 h of incubation; this is the most critical period for the development of PJI (from the time of surgery). However, AgNPs are also known to be cytotoxic in vitro[27,29,31,33] and at high concentrations have neurotoxic effects in vivo.[52] A previous study[20] on AgNP coated titanium

DOI: 10.1021/acsami.7b05150
ACS Appl. Mater. Interfaces 2017, 9, 21169–21180

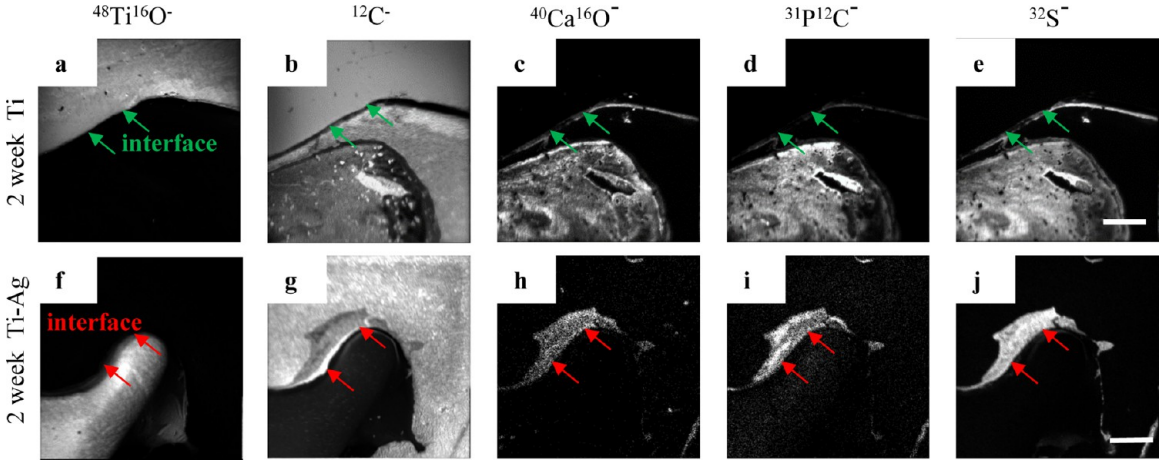

Figure 6. NanoSIMS elemental images of bone−implant interface in (a−e) titanium and (f−j) silver coated titanium implants after two weeks of implantation. The NanoSIMS images (50 × 50 μm^2) were acquired using CAMECA NanoSIMS 50L instrument equipped with Cs^+ primary ion beam. Images reveal the colocalization of sulfur (measured as $^{32}S^-$) and Ca/P (measured as $^{40}Ca^{16}O^-$ and $^{31}P^{12}C^-$, respectively). The arrows highlight the direct contact between the newly formed osseous tissue (measured as $^{40}Ca^{16}O^-$ and $^{31}P^{12}C^-$, respectively) and implants (measured as $^{48}Ti^{16}O^-$) in both groups. Scale bars are 10 μm.

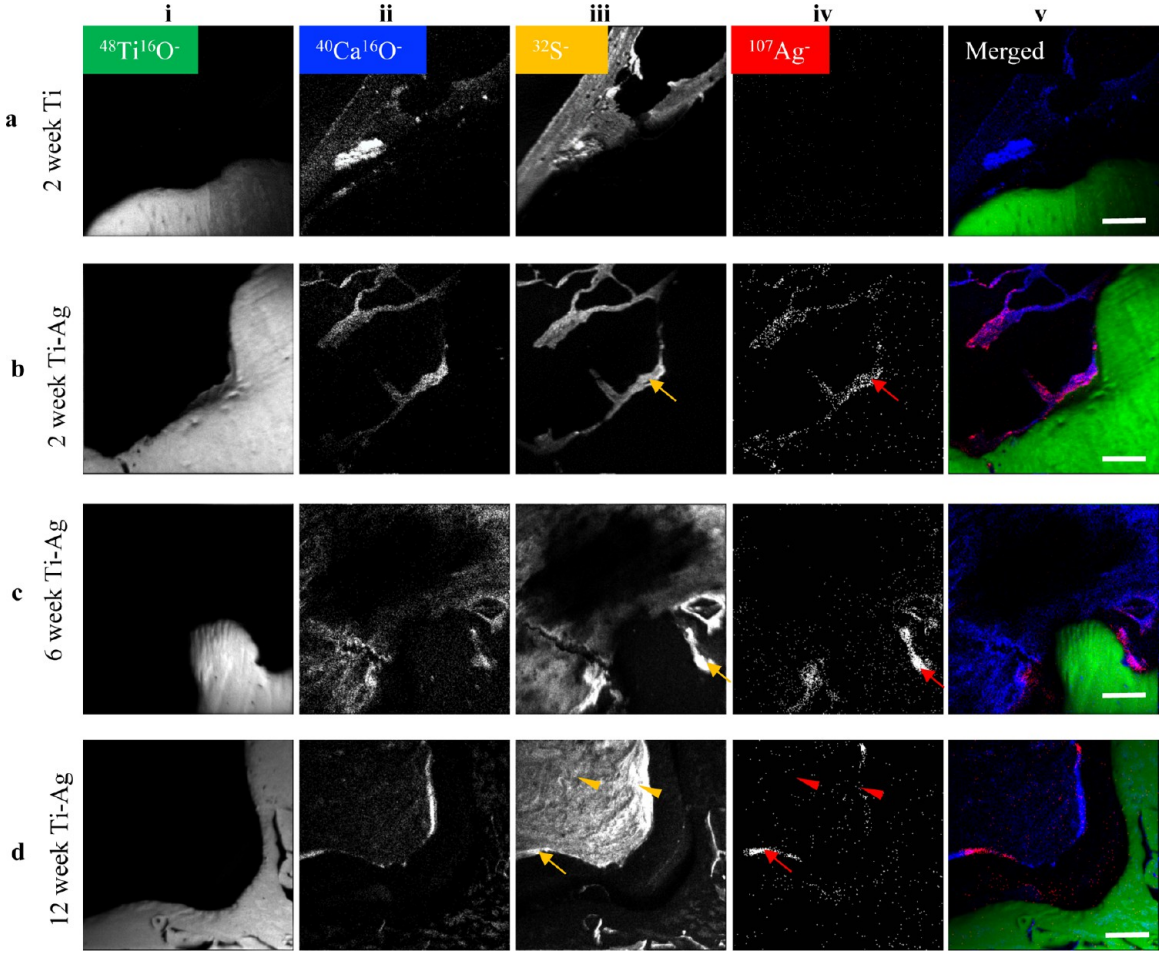

Figure 7. NanoSIMS elemental images of bone−implant interface after (a and b) 2, (c) 6, and (d) 12 weeks of implantation. The NanoSIMS images of $^{48}Ti^{16}O^-$ (i), $^{40}Ca^{16}O^-$ (ii), $^{107}Ag^-$ (iii), $^{32}S^-$ (iv), and merged (v) (superposition of $^{48}Ti^{16}O^-$, $^{40}Ca^{16}O^-$, and $^{107}Ag^-$) were used to determine the uptake of silver. A comparison of images in Ti and Ti−Ag groups at 2 weeks postimplantation (aii, aiv, bii, biv) reveals that the silver (measured as $^{107}Ag^-$) is taken up into the osseous tissue (measured as $^{40}Ca^{16}O^-$). At 2 weeks postimplantation, the NanoSIMS images of $^{107}Ag^-$ (red arrows) and $^{32}S^-$ (yellow arrows) reveal the colocalization of silver and sulfur in the newly formed bone. At 6 and 12 weeks postimplantation, colocalization of $^{107}Ag^-$ (red arrowhead) and $^{32}S^-$ (yellow arrowhead) is observed only at the region near the periphery of the implant. Scale bars are 10 μm.

DOI: 10.1021/acsami.7b05150
ACS Appl. Mater. Interfaces 2017, 9, 21169−21180

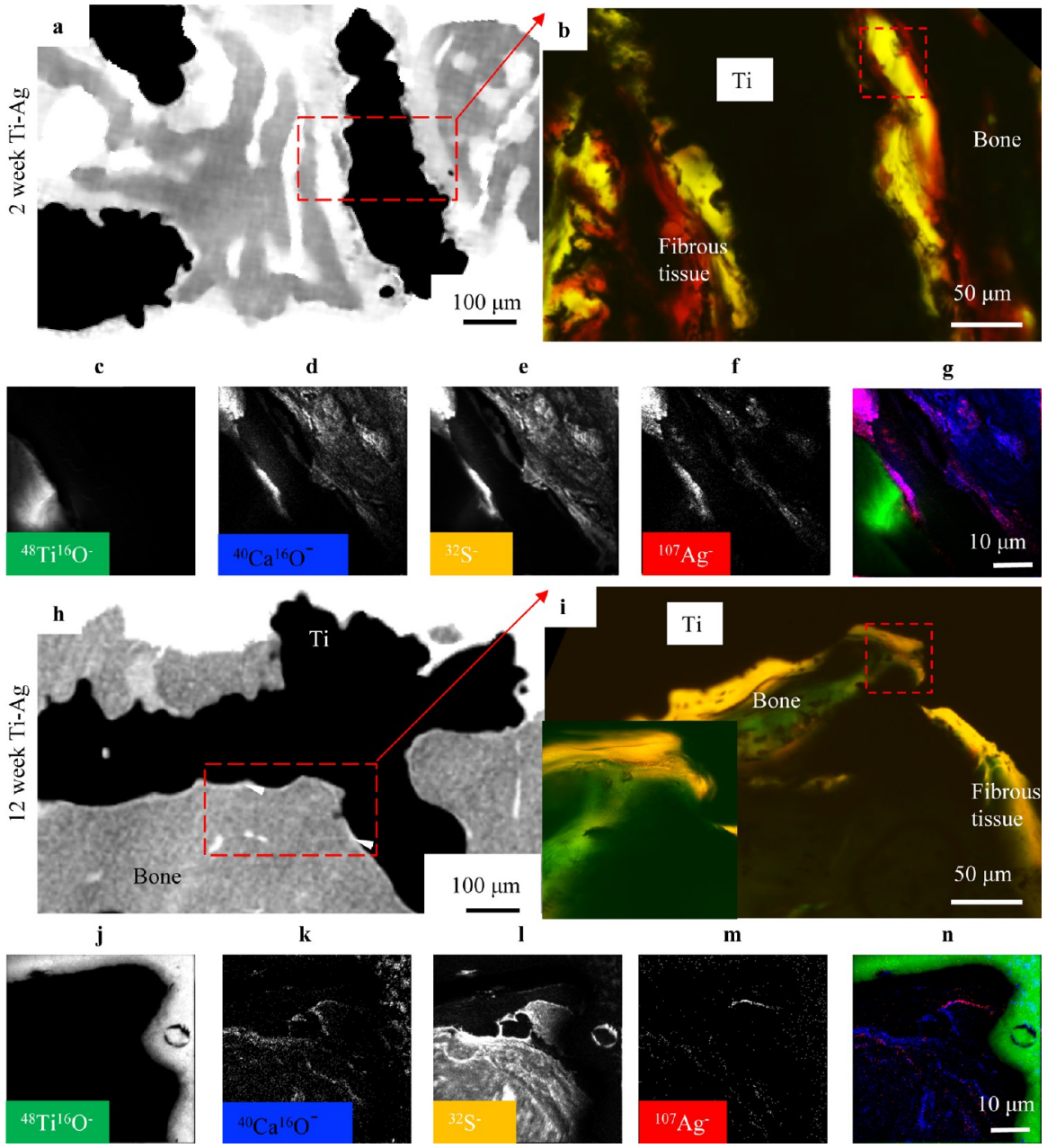

Figure 8. (a–n) Correlative imaging of μCT, Goldners trichrome stained histology, and NanoSIMS show different tissue types and the uptake of silver. At 2 weeks postimplantation, the newly formed bone is observed in both (a) μCT and (b) histology images. Correlative (b) histology and (c–g) NanoSIMS images show the woven bone and fibrous tissue at the bone–implant interface. The colocalization of silver and sulfur occurs in the newly formed woven bone. At 12 weeks postimplantation, the void space of the porous implant is filled with more matured bone, as shown in (h) the μCT image. Correlative (i) histology and NanoSIMS images (j–n) show the lamellar bone and fibrous tissue at the bone–implant interface.

implants showed reduced bacterial (*Staphylococcus epidermidis*) recovery and biofilm formation in vitro. It also showed qualitatively in vivo bone formation and neovascularization within the pores of the implants. Although several studies have reported the use of silver coated devices for orthopedic applications, the uptake/distribution of silver in tissue upon release from an implant and its impact on new bone formation is poorly studied. As nanoscale silver is readily ionized and bioavailable, there is a need to understand the uptake by local osteogenic cells and potentially harmful effects of silver on bone formation. The present study quantifies the impact of AgNP coating on bone formation in addition to determining the nanoscale distribution of silver within tissues adjacent to the AM implant.

AgNPs, via the tissue fluid mediated release of metallic silver particles or Ag^+ ions,[23,29] are known to be involved in the generation of reactive oxygen species,[31] apoptosis,[28] as well as replacing ions that are essential for cellular function (e.g., Ca^{2+} and Mg^{2+}).[33] In the present study, we describe a selective laser melted porous Ti scaffold on which a uniform and metallic nanoparticulate Ag coating was deposited by ALD.[17] Ultrastructural examination of the coating revealed discrete and narrow size distributions (49 ± 3 nm) with no discernible particle aggregation (Figures 1c and d). Growth of ultrathin Ag films (nominal thickness 13 nm, if it were uniform rather than

DOI: 10.1021/acsami.7b05150
ACS Appl. Mater. Interfaces 2017, 9, 21169–21180

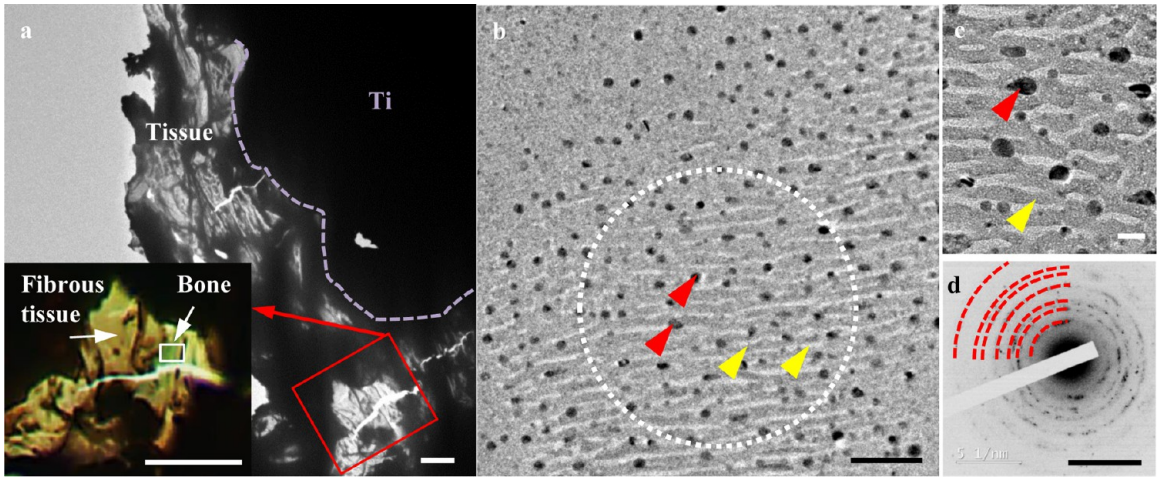

Figure 9. (a) TEM image of a region containing a silver coated titanium scaffold and surrounding tissue at 2 weeks postimplantation. The dotted line delineates the interface between titanium implant and regenerated tissue. Inset (from boxed area) is a histological image of an electron transparent tissue region adjacent to the implant that shows mineralized bone (stained green) next to fibrous connective tissue (stained orange). Higher magnification TEM images (b and c) from the area of bone identified in the inset reveals distinctive ~10 nm width fibrillar structures (yellow arrowheads) and nano-particles (red arrowheads). The association of the fibrillary structures with the electron dense particles is conspicuous (c). SAED pattern of the encircled area in panel b was performed using a selected area aperture size of ~400 nm. The concentric rings (d) imply the presence of a crystalline nanoparticulate phase. The SAED pattern observed matches the standard silver sulfide pattern (dotted arc line in red), strongly supporting the hypothesis that the particles in the TEM images are silver sulfide. Scale bars are 10 μm in panel a and the inset. The other scale bars are (b) 100 nm, (c) 20 nm, and (d) 5 nm^{-1} (in reciprocal space).

particulate islands) allows near atomic scale control over the particle size as well as the total amount of silver in the coating. The impact of AgNPs on biological behavior is both size[27,53] and dose-dependent;[29−31] these results coupled with the complex 3D geometries required for a range of orthopedic implants necessitates an exacting atomic scale control of the silver deposition that can be readily achieved with the ALD process.

Implants and the Extent of Osteogenesis. Here, we show by multimodal correlative imaging techniques and quantitative histological studies at the 2 week time point an equivalent extent of bone ingrowth into the implanted Ti and Ti−Ag scaffolds. Specifically, after 2 weeks, bone ingrowth was observed both within the surface of the scaffold as well as the MC (Figures 2a and b). Normal bone healing is largely mediated by osteogenic cells (principally osteoblasts and osteoclasts) in addition to mesenchymal stem cells provided by the adjacent periosteum and marrow cavity.[54] In the 6 and 12 week samples, less newly formed bone was detected within the marrow cavity (Figures 2c−5f), most likely mediated by osteoclastic resorption on the inner surface of the regenerated cortical bone.[55]

μCT and histology measurements reveal a time-dependent increase in bone formation with and without silver coating, which is associated with a significant decrease in SSA and marked thickening of trabeculae between the 2 and 6 week samples (Figures 2b and c; Figure 4a). Trabecular thickening and areas of contiguous ingrowth within either Ti or Ti−Ag scaffolds is conspicuous, and 2D μCT images reveal pixel intensities that are consistent with adjacent cortical bone from 12 week samples (Figures 2f and g and 3e and f). While correlative imaging techniques employing μCT and histology to quantify bone ingrowth in AM open-porous titanium implant[50] are useful for confirmation of tissue morphology at the micrometer scale, these techniques have neither the resolution nor the sensitivity to investigate nanoscale osseointegration and uptake of metallic ions by regenerating bone. To address this issue, correlative multimodal imaging was further augmented using NanoSIMS and TEM to investigate elemental mapping of the bone−implant interface across multiple length scales. Medium resolution (~10 μm) μCT imaging allowed non-destructive 3D quantification quantity of regenerated bone within the porous implants. The higher resolution (~3 μm) of histological images permits reliable distinguishing of host and regenerated bone in addition to other types of connective tissue. The high lateral spatial resolution (~200 nm) afforded by NanoSIMS allowed mapping with high elemental sensitivity and resolution of thin trabecular bone (~1 μm-thick) in the vicinity of implants (Figures 6a, 7b, and 8g).

Bone growth occurs within the pores of the scaffold via thin trabeculae (Figures 2b and c) as well as directly on the surfaces of Ti and silver coated Ti implants (Figure 6b and g). These two types of bone growth are termed distance (from defect to implant surface) and contact (from implant surface to defect) osteogenesis,[56] respectively, and lead to bone formation in opposite directions and faster osseointegration as evidenced during the 2−12 week time points we examined (Figures 2b−h). The extent of bone growth along titanium surfaces (measured via bone contact percentage; Figure 3g) is not significantly different between the Ti and Ti−Ag groups, indicating that coating of Ti surfaces with AgNPs does not impact osteoconduction within open-porous titanium implants.

Eriksson et al.[57] employed time-of-flight SIMS (TOF-SIMS), finding that, after 4 weeks of implantation in rat tibiae, hydroxyapatite fragments were present at the bone−implant interface. In our study, strong signals from $^{40}Ca^{16}O^-$ and $^{31}P^{12}C^-$ were observed at 2 weeks postimplantation, providing further confirmation of contact osteogenesis on the surface of Ti implants coated with AgNPs.

Silver Nanoparticle Sulfidation in Osseous Tissue. NanoSIMS results indicate that by 2 weeks, silver from the implant surface is released, and local dissemination results in uptake by adjacent osseous tissue (Figure 7b(iv) and Figure 8f).

DOI: 10.1021/acsami.7b05150
ACS Appl. Mater. Interfaces 2017, 9, 21169−21180

Macrophages, the primary phagocytic cell, arrive after 24−72 h at the site of bone injury and are capable of rapidly solubilizing metallic silver extracellularly and then accumulating silver−sulfur nanocrystals within minutes in lysosome-like structures in vitro.[33] A similar process has been observed following ingestion of silver coated nanowires by human type 1 alveolar epithelial cells, suggesting that complexing of silver−sulfur is a possible detoxification mechanism for short-term accumulation of free Ag^+.[34] A recent study demonstrated that the formation of silver sulfide nanocrystals mediated through strongly adsorbed protein coronas on silver nanoparticles leads to reduced toxicity.[35] Because the silver we detected in this study was associated with sulfur, it is likely that a similar pathway of detoxification occurs in regenerated bone tissue adjacent to the implant surface. This mechanism is consistent with our data showing colocalization of silver with sulfur (Figure 7b(v), and our TEM and SAED results showing its biotransformation to silver sulfide nanoparticles (Figures 9b and c and SAED Figure 9d) over large sections of bone tissue. The combined NanoSIMS and TEM/SAED results provide strong evidence of the mechanism by which AgNP detoxification occurs within regenerating bone. The association of silver sulfide only within the osseous tissue could be explained by the abundance of sulfur containing proteins (i.e., albumin)[58] and/or sulfur compounds (i.e., H_2S) generated during tissue formation.[34,59−61]

Because silver sulfide is less soluble than silver ions, the effective antimicrobial activity of the silver-coated implants will be influenced by the biotransformation process. However, further study is required to investigate the efficacy, mode and mechanism of antimicrobial action.

The measured SAED pattern (Figure 9d, dashed red lines) closely matches the theoretical nanocrystalline Ag_2S pattern.[62] However, some elemental silver was also indexed, and unindexed lines suggest the presence of other crystalline species such as hydroxy apatite. In addition to this, artifacts introduced during sample preparation (e.g., material sputtered from other regions) will also complicate the analysis. Distinctive ∼10 nm width fibrillar structures (yellow arrowheads, Figures 9b and c) are also visible, which we hypothesize to be collagen type I, as it is observed in the newly regenerated bone.

In vitro, the uptake of silver is considered harmful due to the internalized AgNPs being released as silver ions,[63] which could generate reactive oxygen species (ROS) and cause cell death.[29] Of significance is that AgNPs are actively endocytosed by numerous human cell types such as mesenchymal stem cells (MSC),[31] alveolar epithelial type I cells,[34] HaCaT keratinocytes,[25] and peripheral blood mononuclear cells (PBMC)[26] consistent with the hypothesis that the endolysomomal compartment is the route for detoxification of silver in vitro. Additionally, it is well-described that the effects of AgNPs are dependent on both their size and cell type being investigated in vitro: for example, low concentrations of smaller size particles (around 50 nm) (similar to the particle size observed on the surface of our ALD coated Ti-implants) are relatively benign in L929 fibroblasts,[28] hMSC,[26,31] human PBMC,[26] and HaCaT keratinocytes.[25] However, at high concentrations, small size AgNPs are toxic, as demonstrated in 2 human osteosarcoma cell lines,[30] mouse primary osteoblast and osteoclasts,[27] and hMSC.[29]

In vivo studies examining administration via various routes (inhalation, intravenous, and intraperitoneal) have also highlighted the importance of dose and AgNP size to their toxicity. Inhalation of lower doses of AgNPs results in no measurable genotoxicity in bone marrow.[64] High doses of orally administered AgNPs result in accumulation in the kidneys as well as liver damage[65] in addition to quantifiable bone marrow cell genotoxicity.[66] Similarly, intravenous or intraperitoneal delivery of a high dose of AgNPs results in an increased frequency of polychromatic erythrocytes in bone marrow,[67] functional suppression of the immune system,[68] or a combined hepatotoxicity and genotoxicity.[69] When AgNPs are dispersed within DL-lactic-*co*-glycolic acid,[70] incorporated into nanotubes,[71,72] or immobilized on Ti[73] prior to implantation into bone, the scaffolds are osteoconductive, well-integrated, and show antimicrobial activity and no evidence of toxicity. Similar to these aforementioned studies, the AgNP particle size we used in our in vivo analysis was both small (∼43 nm average) and restricted to the area of regenerating bone adjacent to the implant, resulting in excellent osseointegration with no signs of toxicity.

5. CONCLUSIONS

Our in vivo experiments enabled the assessment of bone tissue regeneration within an uninfected rat tibia defect in response to an antimicrobial silver nanoparticle surface coating. The silver nanoparticle-coated porous titanium implants showed bone formation and osseointegration comparable to that of the uncoated implants following 2−12 weeks of implantation. Correlative imaging with NanoSIMS, histomorphometry, and 3D X-ray microcomputed tomography was used to analyze silver content in tibiae implanted with these scaffolds. The results demonstrated that silver accumulation primarily occurs within the osseous tissue immediately adjacent to the surface and was colocalized to sulfur. Transmission electron microscopy and selected area electron diffraction patterns reveal the sulfidation of silver, forming less toxic Ag_2S nanoparticles within the newly formed bone.

AUTHOR INFORMATION

Corresponding Author

*E-mail: peter.lee@manchester.ac.uk.

ORCID

Peter D. Lee: 0000-0002-3898-8881

Notes

The authors declare no competing financial interest.

ACKNOWLEDGMENTS

This work was made possible by the facilities and support provided by the University of Manchester and Research Complex at Harwell (RCaH), funded in part by the EPSRC (EP/I02249X/1). The AgNP ALD work was partly funded by EPSRC through the Liverpool Knowledge Transfer Account (EP/H500146/1). We are also grateful for the support and helpful comments provided our colleagues Dr. Kamel Madi, Dr. Yiqiang Wang, Dr. Amy Nommeots-Nomm, and Dr. Robert Atwood together with Dr. Shilei Zhang (Oxford). Data statement: Representative data from the experiments is presented in the graphs in this manuscript; the underlying data is not provided due to its huge size.

REFERENCES

(1) Amin Yavari, S.; Loozen, L.; Paganelli, F. L.; Bakhshandeh, S.; Lietaert, K.; Groot, J. A.; Fluit, A. C.; Boel, C. E.; Alblas, J.; Vogely, H.

DOI: 10.1021/acsami.7b05150
ACS Appl. Mater. Interfaces 2017, 9, 21169−21180

C. Antibacterial Behavior of Additively Manufactured Porous Titanium with Nanotubular Surfaces Releasing Silver Ions. *ACS Appl. Mater. Interfaces* **2016**, *8*, 17080−17089.
(2) Kim, T. B.; Yue, S.; Zhang, Z.; Jones, E.; Jones, J. R.; Lee, P. D. Additive Manufactured Porous Titanium Structures: Through-Process Quantification of Pore and Strut Networks. *J. Mater. Process. Technol.* **2014**, *214*, 2706−2715.
(3) Braem, A.; Chaudhari, A.; Cardoso, M. V.; Schrooten, J.; Duyck, J.; Vleugels, J. Peri-and Intra-Implant Bone Response to Microporous Ti Coatings with Surface Modification. *Acta Biomater.* **2014**, *10*, 986−995.
(4) Xiu, P.; Jia, Z.; Lv, J.; Yin, C.; Cheng, Y.; Zhang, K.; Song, C.; Leng, H.; Zheng, Y.; Cai, H. Tailored Surface Treatment of 3D Printed Porous Ti6Al4V by Microarc Oxidation for Enhanced Osseointegration Via Optimized Bone in-Growth Patterns and Interlocked Bone/Implant Interface. *ACS Appl. Mater. Interfaces* **2016**, *8*, 17964−17975.
(5) Zhang, Z.; Jones, D.; Yue, S.; Lee, P.; Jones, J.; Sutcliffe, C.; Jones, E. Hierarchical Tailoring of Strut Architecture to Control Permeability of Additive Manufactured Titanium Implants. *Mater. Sci. Eng., C* **2013**, *33*, 4055−4062.
(6) Arciola, C. R.; Campoccia, D.; Speziale, P.; Montanaro, L.; Costerton, J. W. Biofilm Formation in Staphylococcus Implant Infections. A Review of Molecular Mechanisms and Implications for Biofilm-Resistant Materials. *Biomaterials* **2012**, *33*, 5967−5982.
(7) Zimmerli, W.; Trampuz, A.; Ochsner, P. E. Prosthetic-Joint Infections. *N. Engl. J. Med.* **2004**, *351*, 1645−1654.
(8) Kaltsas, D. S. Infection after Total Hip Arthroplasty. *Ann. R. Coll. Surg. Engl.* **2004**, *86*, 267.
(9) Meehan, J.; Jamali, A. A.; Nguyen, H. Prophylactic Antibiotics in Hip and Knee Arthroplasty. *J. Bone Joint Surg. Am.* **2009**, *91*, 2480−2490.
(10) Jennison, T.; McNally, M.; Pandit, H. Prevention of Infection in External Fixator Pin Sites. *Acta Biomater.* **2014**, *10*, 595−603.
(11) Römling, U.; Balsalobre, C. Biofilm Infections, Their Resilience to Therapy and Innovative Treatment Strategies. *J. Intern. Med.* **2012**, *272*, 541−561.
(12) Ramalingam, B.; Parandhaman, T.; Das, S. K. Antibacterial Effects of Biosynthesized Silver Nanoparticles on Surface Ultrastructure and Nanomechanical Properties of Gram-Negative Bacteria Viz. Escherichia Coli and Pseudomonas Aeruginosa. *ACS Appl. Mater. Interfaces* **2016**, *8*, 4963−4976.
(13) Eckhardt, S.; Brunetto, P. S.; Gagnon, J.; Priebe, M.; Giese, B.; Fromm, K. M. Nanobio Silver: Its Interactions with Peptides and Bacteria, and Its Uses in Medicine. *Chem. Rev.* **2013**, *113*, 4708−4754.
(14) Schacht, V.; Neumann, L.; Sandhi, S.; Chen, L.; Henning, T.; Klar, P.; Theophel, K.; Schnell, S.; Bunge, M. Effects of Silver Nanoparticles on Microbial Growth Dynamics. *J. Appl. Microbiol.* **2013**, *114*, 25−35.
(15) Feng, Q.; Wu, J.; Chen, G.; Cui, F.; Kim, T.; Kim, J. A Mechanistic Study of the Antibacterial Effect of Silver Ions on Escherichia Coli and Staphylococcus Aureus. *J. Biomed. Mater. Res.* **2000**, *52*, 662−668.
(16) Jung, W. K.; Koo, H. C.; Kim, K. W.; Shin, S.; Kim, S. H.; Park, Y. H. Antibacterial Activity and Mechanism of Action of the Silver Ion in Staphylococcus Aureus and Escherichia Coli. *Appl. Environ. Microbiol.* **2008**, *74*, 2171−2178.
(17) Golrokhi, Z.; Chalker, S.; Sutcliffe, C. J.; Potter, R. J. Self Limiting Atomic Layer Deposition of Conformal Nano-Structured Silver Films. *Appl. Surf. Sci.* **2015**, *364*, 789−797.
(18) Ewald, A.; Glückermann, S. K.; Thull, R.; Gbureck, U. Antimicrobial Titanium/Silver Pvd Coatings on Titanium. *Biomedical Engineering Online* **2006**, *5*, 22.
(19) Zhang, W.; Luo, Y.; Wang, H.; Jiang, J.; Pu, S.; Chu, P. K. Ag and Ag/N 2 Plasma Modification of Polyethylene for the Enhancement of Antibacterial Properties and Cell Growth/Proliferation. *Acta Biomater.* **2008**, *4*, 2028−2036.
(20) Devlin-Mullin, A.; Todd, N. M.; Golrokhi, Z.; Geng, H.; Konerding, M. A.; Ternan, N. G.; Hunt, J. A.; Potter, R. J.; Sutcliffe, C.; Jones, E. Atomic Layer Deposition of a Silver Nanolayer on Advanced Titanium Orthopedic Implants Inhibits Bacterial Colonization and Supports Vascularized De Novo Bone Ingrowth. *Adv. Healthcare Mater.* **2017**, 1 DOI: 10.1002/adhm.201700033.
(21) Brennan, S.; Fhoghlú, C. N.; Devitt, B.; O'Mahony, F.; Brabazon, D.; Walsh, A. Silver Nanoparticles and Their Orthopaedic Applications. *Bone & Joint Journal* **2015**, *97*, 582−589.
(22) Fischer, H. C.; Chan, W. C. Nanotoxicity: The Growing Need for in Vivo Study. *Curr. Opin. Biotechnol.* **2007**, *18*, 565−571.
(23) McShan, D.; Ray, P. C.; Yu, H. Molecular Toxicity Mechanism of Nanosilver. *J. Food Drug Anal.* **2014**, *22*, 116−127.
(24) Milić, M.; Leitinger, G.; Pavičić, I.; Zebić Avdičević, M.; Dobrović, S.; Goessler, W.; Vinković Vrček, I. Cellular Uptake and Toxicity Effects of Silver Nanoparticles in Mammalian Kidney Cells. *J. Appl. Toxicol.* **2015**, *35*, 581−592.
(25) Lu, W.; Senapati, D.; Wang, S.; Tovmachenko, O.; Singh, A. K.; Yu, H.; Ray, P. C. Effect of Surface Coating on the Toxicity of Silver Nanomaterials on Human Skin Keratinocytes. *Chem. Phys. Lett.* **2010**, *487*, 92−96.
(26) Pauksch, L.; Rohnke, M.; Schnettler, R.; Lips, K. S. Silver Nanoparticles Do Not Alter Human Osteoclastogenesis but Induce Cellular Uptake. *Toxicol. Rep.* **2014**, *1*, 900−908.
(27) Albers, C. E.; Hofstetter, W.; Siebenrock, K. A.; Landmann, R.; Klenke, F. M. In Vitro Cytotoxicity of Silver Nanoparticles on Osteoblasts and Osteoclasts at Antibacterial Concentrations. *Nanotoxicology* **2013**, *7*, 30−36.
(28) Park, M. V.; Neigh, A. M.; Vermeulen, J. P.; de la Fonteyne, L. J.; Verharen, H. W.; Briedé, J. J.; van Loveren, H.; de Jong, W. H. The Effect of Particle Size on the Cytotoxicity, Inflammation, Developmental Toxicity and Genotoxicity of Silver Nanoparticles. *Biomaterials* **2011**, *32*, 9810−9817.
(29) Pauksch, L.; Hartmann, S.; Rohnke, M.; Szalay, G.; Alt, V.; Schnettler, R.; Lips, K. S. Biocompatibility of Silver Nanoparticles and Silver Ions in Primary Human Mesenchymal Stem Cells and Osteoblasts. *Acta Biomater.* **2014**, *10*, 439−449.
(30) Hardes, J.; Streitburger, A.; Ahrens, H.; Nusselt, T.; Gebert, C.; Winkelmann, W.; Battmann, A.; Gosheger, G. The Influence of Elementary Silver Versus Titanium on Osteoblasts Behaviour in Vitro Using Human Osteosarcoma Cell Lines. *Sarcoma* **2007**, 1−5.
(31) Sengstock, C.; Diendorf, J.; Epple, M.; Schildhauer, T. A.; Köller, M. Effect of Silver Nanoparticles on Human Mesenchymal Stem Cell Differentiation. *Beilstein J. Nanotechnol.* **2014**, *5*, 2058−2069.
(32) Wu, A. C.; Raggatt, L. J.; Alexander, K. A.; Pettit, A. R. Unraveling Macrophage Contributions to Bone Repair. *BoneKEy Rep* **2013**, *2*, 1.
(33) Locht, L. J.; Larsen, A.; Stoltenberg, M.; Danscher, G. Cultured Macrophages Cause Dissolucytosis of Metallic Silver. *Histol. Histopathol.* **2009**, *24*, 167.
(34) Chen, S.; Goode, A. E.; Sweeney, S.; Theodorou, I. G.; Thorley, A. J.; Ruenraroengsak, P.; Chang, Y.; Gow, A.; Schwander, S.; Skepper, J. Sulfidation of Silver Nanowires inside Human Alveolar Epithelial Cells: A Potential Detoxification Mechanism. *Nanoscale* **2013**, *5*, 9839−9847.
(35) Miclăuş, T.; Beer, C.; Chevallier, J.; Scavenius, C.; Bochenkov, V. E.; Enghild, J. J.; Sutherland, D. S. Dynamic Protein Coronas Revealed as a Modulator of Silver Nanoparticle Sulphidation in Vitro. *Nat. Commun.* **2016**, *7*, 1.
(36) Albrektsson, T.; Johansson, C. Osteoinduction, Osteoconduction and Osseointegration. *Eur. Spine J.* **2001**, *10*, S96−S101.
(37) Stevens, M. M. Biomaterials for Bone Tissue Engineering. *Mater. Today* **2008**, *11*, 18−25.
(38) Webster, T. J.; Patel, A. A.; Rahaman, M.; Bal, B. S. Anti-Infective and Osteointegration Properties of Silicon Nitride, Poly (Ether Ether Ketone), and Titanium Implants. *Acta Biomater.* **2012**, *8*, 4447−4454.
(39) Einhorn, T. A.; Gerstenfeld, L. C. Fracture Healing: Mechanisms and Interventions. *Nat. Rev. Rheumatol.* **2014**, *11*, 45−54.
(40) Korani, M.; Rezayat, S. M.; Arbabi Bidgoli, S. Sub-Chronic Dermal Toxicity of Silver Nanoparticles in Guinea Pig: Special

Emphasis to Heart, Bone and Kidney Toxicities. *Iran. J. Pharm. Res.* **2013**, *12*, 511−519.
(41) Marsich, E.; Travan, A.; Donati, I.; Turco, G.; Kulkova, J.; Moritz, N.; Aro, H.; Crosera, M.; Paoletti, S. Biological Responses of Silver-Coated Thermosets: An in Vitro and in Vivo Study. *Acta Biomater.* **2013**, *9*, 5088−5099.
(42) Qin, H.; Cao, H.; Zhao, Y.; Jin, G.; Cheng, M.; Wang, J.; Jiang, Y.; An, Z.; Zhang, X.; Liu, X. Antimicrobial and Osteogenic Properties of Silver-Ion-Implanted Stainless Steel. *ACS Appl. Mater. Interfaces* **2015**, *7*, 10785−10794.
(43) Mullen, L.; Stamp, R. C.; Fox, P.; Jones, E.; Ngo, C.; Sutcliffe, C. J. Selective Laser Melting: A Unit Cell Approach for the Manufacture of Porous, Titanium, Bone in-Growth Constructs, Suitable for Orthopedic Applications. Ii. Randomized Structures. *J. Biomed. Mater. Res., Part B* **2010**, *92*, 178−188.
(44) Chalker, P.; Romani, S.; Marshall, P.; Rosseinsky, M.; Rushworth, S.; Williams, P. Liquid Injection Atomic Layer Deposition of Silver Nanoparticles. *Nanotechnology* **2010**, *21*, 405602.
(45) Della Valle, C.; Visai, L.; Santin, M.; Cigada, A.; Candiani, G.; Pezzoli, D.; Arciola, C. R.; Imbriani, M.; Chiesa, R. A Novel Antibacterial Modification Treatment of Titanium Capable to Improve Osseointegration. *Int. J. Artif. Organs* **2012**, *35*, 864−875.
(46) Otsu, N. A Threshold Selection Method from Gray-Level Histograms. *IEEE Trans. on Sys. Man and Cybernetics* **1979**, *9*, 62−65.
(47) Chao, S. M.; Tsai, D. M.; Chiu, W. Y.; Li, W. C. Anisotropic Diffusion-Based Detail-Preserving Smoothing for Image Restoration. In *2010 17th IEEE International Conference on Image Processing (ICIP)*; IEEE: Hong Kong, 2010; pp 4145−4148.
(48) Parfitt, A. M.; Drezner, M. K.; Glorieus, F. H.; Kanis, J. A.; Malluche, H.; Meunier, P. J.; Ott, S. M.; Recker, R. R. Bone Histomorphometry: Standardization of Nomenclature, Symbols, and Units. *J. Bone Miner. Res.* **1987**, *2*, 595−610.
(49) Atwood, R.; Jones, J.; Lee, P.; Hench, L. Analysis of Pore Interconnectivity in Bioactive Glass Foams Using X-Ray Microtomography. *Scr. Mater.* **2004**, *51*, 1029−1033.
(50) Geng, H.; Todd, N. M.; Devlin-Mullin, A.; Poologasundarampillai, G.; Kim, T. B.; Madi, K.; Cartmell, S.; Mitchell, C. A.; Jones, J. R.; Lee, P. D. A Correlative Imaging Based Methodology for Accurate Quantitative Assessment of Bone Formation in Additive Manufactured Implants. *J. Mater. Sci.: Mater. Med.* **2016**, *27*, 1−9.
(51) Rentsch, C. Comprehensive Histological Evaluation of Bone Implants. *Biomatter* **2014**, *4*, e27993.
(52) Chandirasekar, S.; Chandrasekaran, C.; Muthukumarasamyvel, T.; Sudhandiran, G.; Rajendiran, N. Sodium Cholate-Templated Blue Light-Emitting Ag Subnanoclusters: In Vivo Toxicity and Imaging in Zebrafish Embryos. *ACS Appl. Mater. Interfaces* **2015**, *7*, 1422−1430.
(53) Chen, L. Q.; Fang, L.; Ling, J.; Ding, C. Z.; Kang, B.; Huang, C. Z. Nanotoxicity of Silver Nanoparticles to Red Blood Cells: Size Dependent Adsorption, Uptake, and Hemolytic Activity. *Chem. Res. Toxicol.* **2015**, *28*, 501−509.
(54) Mizuno, K.; Mineo, K.; Tachibana, T.; Sumi, M.; Matsubara, T.; Hirohata, K. The Osteogenetic Potential of Fracture Haematoma. Subperiosteal and Intramuscular Transplantation of the Haematoma. *J. Bone Jt. Surg., Br. Vol.* **1990**, *72*, 822−829.
(55) Teitelbaum, S. L. Bone Resorption by Osteoclasts. *Science* **2000**, *289*, 1504−1508.
(56) Davies, J. E. Understanding Peri-Implant Endosseous Healing. *J. Dent. Educ.* **2003**, *67*, 932−949.
(57) Eriksson, C.; Malmberg, P.; Nygren, H. Time-of-Flight Secondary Ion Mass Spectrometric Analysis of the Interface between Bone and Titanium Implants. *Rapid Commun. Mass Spectrom.* **2008**, *22*, 943−949.
(58) Yadav, M.; Singh, A.; Ali, S.; Rizivi, N.; Hussain, S. R.; Kumar, V. Role of Serum Albumin in Fracture Healing. *Int. J. Biomed. Res.* **2015**, *6*, 452−455.
(59) Lin, V. S.; Lippert, A. R.; Chang, C. J. Cell-Trappable Fluorescent Probes for Endogenous Hydrogen Sulfide Signaling and Imaging H2o2-Dependent H2s Production. *Proc. Natl. Acad. Sci. U. S. A.* **2013**, *110*, 7131−7135.
(60) Waer, S. M. The Effect of Some Metal Ions on Volatile Sulfur-Containing Compounds Originating from the Oral Cavity. *Acta Odontol. Scand.* **1997**, *55*, 261−264.
(61) Drake, P. L.; Hazelwood, K. J. Exposure-Related Health Effects of Silver and Silver Compounds: A Review. *Ann. Occup. Hyg.* **2005**, *49*, 575−585.
(62) Frueh, A. J. The Crystallography of Silver Sulfide, Ag2s. *Zeitschrift für Kristallographie-Crystalline Materials* **1958**, *110*, 136−144.
(63) Hsiao, I.-L.; Hsieh, Y.-K.; Wang, C.-F.; Chen, I.-C.; Huang, Y.-J. Trojan-Horse Mechanism in the Cellular Uptake of Silver Nanoparticles Verified by Direct Intra-and Extracellular Silver Speciation Analysis. *Environ. Sci. Technol.* **2015**, *49*, 3813−3821.
(64) Kim, J. S.; Sung, J. H.; Ji, J. H.; Song, K. S.; Lee, J. H.; Kang, C. S.; Yu, I. J. In Vivo Genotoxicity of Silver Nanoparticles after 90-Day Silver Nanoparticle Inhalation Exposure. *SH W* **2011**, *2*, 34−38.
(65) Kim, Y. S.; Kim, J. S.; Cho, H. S.; Rha, D. S.; Kim, J. M.; Park, J. D.; Choi, B. S.; Lim, R.; Chang, H. K.; Chung, Y. H. Twenty-Eight-Day Oral Toxicity, Genotoxicity, and Gender-Related Tissue Distribution of Silver Nanoparticles in Sprague-Dawley Rats. *Inhalation Toxicol.* **2008**, *20*, 575−583.
(66) Patlolla, A. K.; Hackett, D.; Tchounwou, P. B. Genotoxicity Study of Silver Nanoparticles in Bone Marrow Cells of Sprague−Dawley Rats. *Food Chem. Toxicol.* **2015**, *85*, 52−60.
(67) Dobrzyńska, M. M.; Gajowik, A.; Radzikowska, J.; Lankoff, A.; Dušinská, M.; Kruszewski, M. Genotoxicity of Silver and Titanium Dioxide Nanoparticles in Bone Marrow Cells of Rats in Vivo. *Toxicology* **2014**, *315*, 86−91.
(68) Vandebriel, R. J.; Tonk, E. C.; de la Fonteyne-Blankestijn, L. J.; Gremmer, E. R.; Verharen, H. W.; van der Ven, L. T.; van Loveren, H.; de Jong, W. H. Immunotoxicity of Silver Nanoparticles in an Intravenous 28-Day Repeated-Dose Toxicity Study in Rats. *Part. Fibre Toxicol.* **2014**, *11*, 21.
(69) El Mahdy, M. M.; Eldin, T. A. S.; Aly, H. S.; Mohammed, F. F.; Shaalan, M. I. Evaluation of Hepatotoxic and Genotoxic Potential of Silver Nanoparticles in Albino Rats. *Exp. Toxicol. Pathol.* **2015**, *67*, 21−29.
(70) Liu, Y.; Zheng, Z.; Zara, J. N.; Hsu, C.; Soofer, D. E.; Lee, K. S.; Siu, R. K.; Miller, L. S.; Zhang, X.; Carpenter, D. The Antimicrobial and Osteoinductive Properties of Silver Nanoparticle/Poly (Dl-Lactic-Co-Glycolic Acid)-Coated Stainless Steel. *Biomaterials* **2012**, *33*, 8745−8756.
(71) Cheng, H.; Li, Y.; Huo, K.; Gao, B.; Xiong, W. Long-Lasting in Vivo and in Vitro Antibacterial Ability of Nanostructured Titania Coating Incorporated with Silver Nanoparticles. *J. Biomed. Mater. Res., Part A* **2014**, *102*, 3488−3499.
(72) Cheng, H.; Xiong, W.; Fang, Z.; Guan, H.; Wu, W.; Li, Y.; Zhang, Y.; Alvarez, M. M.; Gao, B.; Huo, K. Strontium (Sr) and Silver (Ag) Loaded Nanotubular Structures with Combined Osteoinductive and Antimicrobial Activities. *Acta Biomater.* **2016**, *31*, 388−400.
(73) Zhu, Y.; Cao, H.; Qiao, S.; Wang, M.; Gu, Y.; Luo, H.; Meng, F.; Liu, X.; Lai, H. Hierarchical Micro/Nanostructured Titanium with Balanced Actions to Bacterial and Mammalian Cells for Dental Implants. *Int. J. Nanomed.* **2015**, *10*, 6659.

DOI: 10.1021/acsami.7b05150
ACS Appl. Mater. Interfaces 2017, 9, 21169−21180